PCCP

PAPER

View Article Online
View Journal | View Issue

Check for updates

Cite this: *Phys. Chem. Chem. Phys.*, 2019, **21**, 24976

Near dissociation states for H_2^+–He on MRCI and FCI potential energy surfaces†

Debasish Koner,[a] Juan Carlos San Vicente Veliz,[a] Ad van der Avoird[b] and Markus Meuwly*[a]

Received 24th September 2019,
Accepted 22nd October 2019

DOI: 10.1039/c9cp05259c

rsc.li/pccp

New potential energy surfaces (PES) have been constructed for H_2^+–He using a reproducing kernel Hilbert space (RKHS) representation from an extensive number of *ab initio* energies computed at the multi reference and full configuration interaction levels of theory. For the MRCI PES the long-range interaction region of the PES is described by analytical functions and is connected smoothly to the short range interaction region, represented as a RKHS. All bound ro-vibrational states for the ground electronic state of H_2^+–He are calculated using two different methods to determine quantum bound states. Comparing transition frequencies for the near-dissociation states for *ortho*- and *para*-H_2^+–He allows assignment of the 15.2 GHz line to a J = 2 e/f parity doublet of *ortho*-H_2^+–He whereas the experimentally determined 21.8 GHz line is only consistent with a (J = 0) → (J = 1) e/e transition in *para*-H_2^+–He.

I. Introduction

The interaction between ions and neutral atoms or molecules is of central importance in atmospheric and astronomical processes and environments. Prominent species in the interstellar environment include H_3^+, CH_2^+, HCO^+ and N_2H^+, among others.[1] Additionally, ions are also considered to play an important role in the formation of atmospheric aerosols.[2]

Very recently,[3] the HeH^+ ion, which was the first molecule of the primordial universe,[4] has been detected in interstellar space and means for the direct detection of H_2^+ have been discussed.[5] However, although H_2^+ is most likely formed and present in space, *e.g.* through the $HeH^+ + H \rightarrow H_2^+ + He$ reaction,[3] (which is believed to be the first atom–diatom reaction in the universe[6]) collisions with H and H_2 are also important loss channels of the ion. Nevertheless, with H_2^+ present in the interstellar medium, it is also likely that the H_2^+–He complex is formed. Hence, H_2^+–He plays an important role already in the early stages of the Molecular Universe.

The interaction between He and H_2^+ is also important for the rotational cooling of H_2^+ through collisions with Helium as the buffer gas.[7] This is an attractive way to generate translationally and internally cold H_2^+ ions suitable for precision measurements.[8,9] With even further increased precision and quantum state control of the ions, fundamental natural constants such as the ratio of the electron to the proton mass, m_e/m_p, can be determined with unprecedented accuracy.

Another process of interest which has been recently investigated is the Penning ionization of ^3S excited He colliding with H_2.[10] This process produces H_2^+–He with sufficient energy to dissociate into ground state and rovibrationally excited He and H_2^+ fragments. Such rovibrationally inelastic half-collisions are particularly sensitive to the long-range part of the intermolecular potential, which is dominated by polarization interactions induced by the charge and quadrupole of H_2^+. Furthermore, several long-range states for H_2^+–He have been characterized from microwave spectroscopy and by using electric field extraction.[11,12] However, the interpretation of these spectra has remained elusive, in part due to the limited accuracy of the available potential energy surfaces.

In the past, several PESs have been constructed at different levels of theory to investigate the spectroscopy and dynamics of the H_2^+–He complex.[13–18] To characterize spectral transitions in the microwave region, an accurate long-range potential is required.[14,15] However, the level of theory used for the electronic structure calculations in these earlier efforts was rather modest by today's standards. Full configuration interaction (FCI) with the cc-pVQZ basis has been used more recently but no explicit analytical representation was included.[17] Later, using the *ab initio* data of ref. 17 a new PES was constructed by including an explicit analytical formula only for the diatomic potentials.[18]

In the present work high-level electronic structure methods combined with advanced representation techniques for global potential energy surfaces and accurate representation of the

---

[a] *Department of Chemistry, University of Basel, Klingelbergstrasse 80, CH-4056 Basel, Switzerland. E-mail: m.meuwly@unibas.ch*

[b] *Theoretical Chemistry, Institute for Molecules and Materials, Radboud University Nijmegen, Nijmegen, The Netherlands*

† Electronic supplementary information (ESI) available. See DOI: 10.1039/c9cp05259c

long-range potential are used. With these PESs quantum calculations of all bound states of H_2^+–He with H_2^+ in its ground electronic and vibrational state are then carried out. As the near-dissociative states are particularly sensitive to the long range part of the PES, two different, advanced electronic structure techniques are used: Multireference configuration interaction (MRCI) with Davidson correction (+Q) and full configuration interaction calculations, in order to compare their performance. Also, both PESs are augmented with the analytical long range electrostatics for validating the long-range part computed with the two electronic structure methods. First, the computational methods are presented, followed by the discussion of the bound states computed and their interpretation in view of the near-dissociative states.

II. Computational methods

A. The potential energy surfaces

Two different levels of theory – (a) multi reference configuration interaction level including the Davidson correction (MRCI+Q)[19,20] with the augmented Dunning-type correlation consistent polarized hexaple zeta (aug-cc-pV6Z)[21] basis set and (b) full configuration interaction[22,23] with the augmented Dunning type correlation consistent polarized quintuple zeta (aug-cc-pV5Z)[24,25] basis set – are used in the present work to calculate the *ab initio* energies. Initial orbitals for the MRCI calculations were obtained using the complete active space self-consistent field (CASSCF)[26–28] method with three 1s orbitals of H and He in the active space. The Molpro[29] software was used to perform all electronic structure calculations.

The grids for the *ab initio* energy calculations are set up in Jacobi coordinates (R,r,θ). Here, r is the H_2^+ bond length, R is the distance between He and the center of mass of the H_2^+ ion, and θ is the angle between $\vec{r}$ and $\vec{R}$. The angular grid is defined by Gauss-Legendre quadrature points chosen in the range between $0 \leq \theta \leq 90^\circ$ given the spatial symmetry of the system. Details of the angular and radial grids for the MRCI+Q and FCI calculations are given in Tables S1 and S2 in the ESI.†

The complete adiabatic surface for H_2^+–He can be expressed as a many-body expansion[30]

$$\begin{aligned} &V_{\mathrm{HeHH'}}(r_{\mathrm{HeH}}, r_{\mathrm{HeH'}}, r_{\mathrm{HH'}}) \\ &= V^{(1)}_{\mathrm{He}} + V^{(1)}_{\mathrm{H}} + V^{(1)}_{\mathrm{H^+}} \\ &+ V^{(2)}_{\mathrm{HeH^+}}(r_{\mathrm{HeH}}) + V^{(2)}_{\mathrm{HeH'^+}}(r_{\mathrm{HeH'}}) + V^{(2)}_{\mathrm{HH'^+}}(r_{\mathrm{HH'}}) \\ &+ V^{(3)}(r_{\mathrm{HeH}}, r_{\mathrm{HeH'}}, r_{\mathrm{HH'}}), \end{aligned} \tag{1}$$

where r_{HeH}, $r_{\mathrm{HeH'}}$ and $r_{\mathrm{HH'}}$ are the distances between the respective atoms, and $V_{\mathrm{HeHH'}}(r_{\mathrm{HeH}},r_{\mathrm{HeH'}},r_{\mathrm{HH'}})$ is the total energy of the triatomic system at the corresponding geometry. The $V^{(1)}_i$ are the atomic energies, whereas the $V^{(2)}_i(r_i)$ and $V^{(3)}(r_{\mathrm{HeH}},r_{\mathrm{HeH'}},r_{\mathrm{HH'}})$ are the two- and three-body interaction energies, respectively, at corresponding configurations.

In general, two body interaction energies, *i.e.*, the diatomic potential, for a molecule AB can be expressed as[18,31]

$$V^{(2)}_{\mathrm{AB}}(R_{\mathrm{AB}}) = \frac{c_0 \mathrm{e}^{-\alpha_{\mathrm{AB}} R_{\mathrm{AB}}}}{R_{\mathrm{AB}}} + \sum_{i=1}^{M} c_i \rho^i_{\mathrm{AB}} + V_{\mathrm{long}}(\tilde{r}), \tag{2}$$

with $c_0 > 0$ to ensure $V_{\mathrm{AB}}(R_{\mathrm{AB}}) \rightarrow \infty$ at $R_{\mathrm{AB}} \rightarrow 0$ and $\rho_{\mathrm{AB}} = R_{\mathrm{AB}}\mathrm{e}^{-\beta^{(2)}_{\mathrm{AB}} R_{\mathrm{AB}}}$. The long range part, $V_{\mathrm{long}}(\tilde{r})$, can be written as[14]

$$V_{\mathrm{long}}(\tilde{r}) = -\frac{\alpha_{\mathrm{d}} q^2}{2\tilde{r}^4} - \frac{\alpha_{\mathrm{q}} q^2}{2\tilde{r}^6} - \frac{\alpha_{\mathrm{o}} q^2}{2\tilde{r}^8} - \frac{\beta_{\mathrm{ddq}} q^3}{6\tilde{r}^7} - \frac{\gamma_{\mathrm{d}} q^4}{24\tilde{r}^8}, \tag{3}$$

where q is the charge, and α_{d}, α_{q} and α_o are the dipole, quadrupole and octopole polarizabilities for H and He, respectively. β_{ddq} and γ_{d} are the first and second hyperpolarizabilities, respectively. The values for the polarizabilities of He and H are taken from ref. 14 and 32 and $\tilde{r}$ is defined as[33]

$$\tilde{r} = r + r_{\mathrm{l}} \exp^{(-(r-r_{\mathrm{e}}))}, \tag{4}$$

to remove the divergence of the long range terms at short H–H and H–He separations. Here, r_{l} is a distance parameter and r_{e} is the equilibrium bond distance of the diatomic molecule. The parameters used in this work to obtain the diatomic potentials are given in Table 1.

The linear parameters c_i and the nonlinear parameters α_{AB} and $\beta^{(2)}_{\mathrm{AB}}$ in eqn (3) are determined by fitting the expression with the *ab initio* energies using the Levenberg–Marquardt nonlinear multidimensional fitting method.[34] The optimized linear and nonlinear parameters for the diatomic potentials calculated *via* fitting are given in Tables S3 and S4 (ESI†).

The three-body interaction energies, $V^{(3)}(r_{\mathrm{HeH}},r_{\mathrm{HeH'}},r_{\mathrm{HH'}}) = V^{(3)}(r,R,\theta)$ are calculated from eqn (1). For a particular configuration of H_2^+–He, $V^{(3)}(r,R,\theta)$ can be calculated using the reproducing kernel Hilbert space[35] (RKHS) approach.

The procedure for computing the analytical energy of a given configuration from a set of known *ab initio* energies is briefly described here. According to the RKHS theorem, the value of a function $f(\mathbf{x})$ can be evaluated from a set of known values $f(\mathbf{x}_i)$ at positions $\mathbf{x}_i$ as a linear combination of kernel products

$$\tilde{f}(\mathbf{x}) = \sum_{i=1}^{N} c_i K(\mathbf{x}, \mathbf{x}_i), \tag{5}$$

where c_i are the coefficients and $K(\mathbf{x},\mathbf{x}_i)$ are the reproducing kernels. The coefficients are calculated from the known values

Table 1 Parameters used in the diatomic potentials. All values are in atomic units

	H	He
Dipole polarizability α_{d}	4.5	1.384
Quadrupole polarizability α_{q}	15.0	2.275
Octopole polarizability α_{o}	131.25	10.620
First hyperpolarizability β_{ddq}	159.75	20.41
Second hyperpolarizability γ_{d}	1333.125	37.56

	H_2^+	HeH^+
r_{l}	10.0	8.0
r_{eq}	2.005815	1.4633

by solving a set of linear equations

$$f(\mathbf{x}_j) = \sum_{i=1}^{N} c_i K(\mathbf{x}_i, \mathbf{x}_j). \tag{6}$$

Here it is worth mentioning that the RKHS approach exactly reproduces the input data at the reference points. The derivatives of $\tilde{f}(\mathbf{x})$ can be calculated analytically from the kernel functions $K(\mathbf{x},\mathbf{x}')$. For a multidimensional function the D-dimensional kernel can be constructed as the product of D 1-dimensional kernels $k(x,x')$

$$K(\mathbf{x}, \mathbf{x}') = \prod_{d=1}^{D} k^{(d)}(x^{(d)}, x'^{(d)}), \tag{7}$$

where $k^{(d)}(x^{(d)},x'^{(d)})$ are the 1-dimensional kernels for d-th dimensions.

For the radial dimensions (r and R) a reciprocal power decay kernel[35]

$$k^{[2,4]}(x, x') = \frac{2}{15}\frac{1}{x_>^5} - \frac{2}{21}\frac{x_<}{x_>^6}, \tag{8}$$

is used in the present work where, $x_>$ and $x_<$ are the larger and smaller values of x and x'. The value of this kernel smoothly decays to zero according to x^{-4} as the leading term in the asymptotic region, which gives the correct long-range behavior for atom–diatom type interactions. For the angular dimension, a Taylor spline kernel

$$k^{[2]}(z, z') = 1 + z_< z_> + 2z_<^2 z_> - \frac{2}{3}x_<^3, \tag{9}$$

is used, where $z_>$ and $z_<$ are analogous to $x_>$ and $x_<$. Here, the variable z is defined as

$$z = \frac{1 - \cos\theta}{2}, \tag{10}$$

so that the values of z are always in the interval [0,1].

Finally, the 3-dimensional kernel is

$$K(\mathbf{x},\mathbf{x}') = k^{[2,4]}(R,R')k^{[2,4]}(r,r')k^{[2]}(z,z'), \tag{11}$$

where, $\mathbf{x}$, $\mathbf{x}'$ are (R,r,z) and (R',r',z'), respectively. A computationally efficient toolkit is used in this work to calculate the coefficients and in evaluating the function.[36] Adding a small regularization parameter (here $\lambda = 10^{-19}$) to the diagonal elements provides additional numerical stability. In practice, λ is increased until a regular solution is obtained for the inversion.

To represent the long range part of the H_2^+–He interaction the analytical form from ref. 14

$$\begin{aligned} &V_{\mathrm{long}}(R, r, \theta) \\ &= -\frac{\alpha_{\mathrm{d}} q^2}{2R^4} - \frac{\alpha_{\mathrm{q}} q^2}{2R^6} - \frac{\alpha_0 q^2}{2R^8} - \frac{\beta_{\mathrm{ddq}} q^3}{6R^7} - \frac{\gamma_{\mathrm{d}} q^4}{24R^8} \\ &- \frac{3\alpha_{\mathrm{d}} q \Theta(r) P_2(\cos\theta)}{R^6} - \frac{5\alpha_{\mathrm{d}} q \Phi(r) P_4(\cos\theta)}{R^8} - \frac{6\alpha_{\mathrm{q}} q \Theta(r) P_2(\cos\theta)}{R^8} \\ &- \frac{C_6^0(r) + C_6^2(r) P_2(\cos\theta)}{R^6} - \frac{C_8^0(r) + C_8^2(r) P_2(\cos\theta)}{R^8} \end{aligned} \tag{12}$$

is used. Here, the first five terms represent the charge + induced multipole interactions, the sixth term represents the dipole + quadrupole induction interaction and the seventh and eighth terms represent the higher order induced-dipole + hexadecapole and induced-quadrupole + quadrupole interactions, respectively. Here, $\Theta(r)$ and $\Phi(r)$ are the quadrupole and hexadecapole moments of H_2^+, respectively. The last two terms in eqn (12) are the contributions from dispersion interactions. The r-dependence of the moments and dispersion coefficients is included by representing them as a second degree Taylor series. All parameters used in eqn (12) are those from ref. 14. The parameters for He are given in Table 1.

For configurations with $R \gtrsim 9.0\ a_0$ the MRCI+Q/aug-cc-pV6Z calculations are discontinuous along the R-coordinate, see Fig. 1, where MRCI+Q/aug-cc-pV6Z energies are given fixed values of θ and r. For large values of R, MRCI+Q/aug-cc-pV6Z energies are discontinuous which originates from the Davidson correction of the MRCI energies because the order of the states along a potential energy scan can swap. This then leads to discontinuities in the Davidson-corrected energies. Hence, for the long range part of the PES the explicit analytical long-range expression (see eqn (12)) was used to construct the full 3D PES which is referred to as MRCI+Q+LR in the following. In order to smoothly connect the short- and long-range parts of the MRCI+Q PES a Fermi (switching) function is used (see also ref. 37 for a different switching function), see Fig. 2

$$f_{\mathrm{s}}(R) = \frac{1}{\exp\dfrac{R - R_0}{\delta R} + 1} \tag{13}$$

where $R_0 = 8.5\ a_0$ and $\delta R = 0.2\ a_0$. The function has a value of 0.5 at $R = 8.5\ a_0$. The total potential (V_{tot}) is then calculated as

$$V_{\mathrm{tot}} = f_{\mathrm{s}} V_{\mathrm{RKHS}} + (1 - f_{\mathrm{s}}) V_{\mathrm{long}}, \tag{14}$$

where V_{RKHS} is the short range part of the interaction potential obtained from RKHS interpolation using the many body expansion and $V_{\mathrm{long}} = V_{\mathrm{long}}(R,r,\theta) + V_{H_2^+}(r)$.

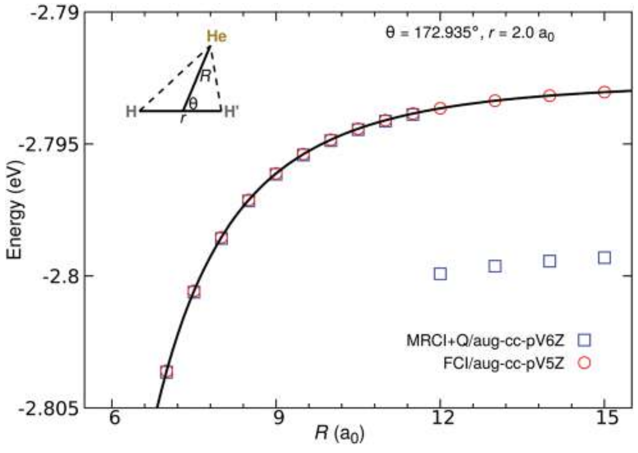

Fig. 1 MRCI+Q/aug-cc-pV6Z and FCI/aug-cc-pV5Z energies as a function of R for fixed θ = 172.935° and r = 2.0 a_0. The black line is the RKHS interpolation of the FCI energies.

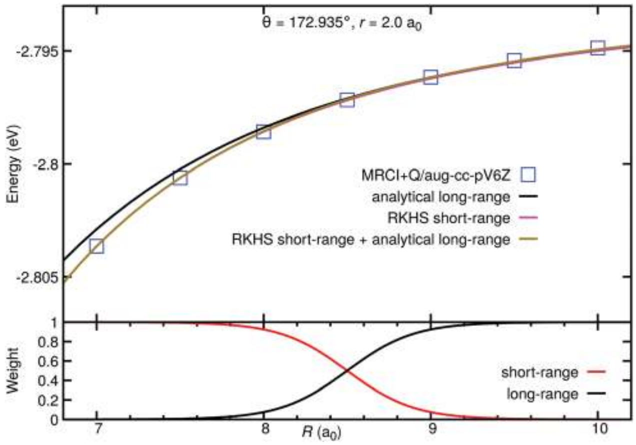

Fig. 2 Upper panel: energies obtained from MRCI+Q/aug-cc-pV6Z, RKHS, analytical long-range and RKHS+analytical are plotted as a function of R for fixed $\theta = 172.935^\circ$ and $r = 2.0\ a_0$. Lower panel: the weights for the short range interaction energies and long range interaction energies as a function of R.

Full CI calculations are smooth out to $R \sim 50\ a_0$, contrary to MRCI+Q, see Fig. 1. Hence, the full 3-dimensional PES was also calculated using FCI using a somewhat smaller basis set, *i.e.*, aug-cc-pV5Z. This PES, called FCI in the following, was again represented as a RKHS. Although the FCI energies are smooth in the R-long range, a third PES (FCI+LR) was constructed by using the same long range expression used for the MRCI+Q+LR PES. For the FCI+LR PES the parameter values in the switching function were $R_0 = 13.5\ a_0$ and $\delta R = 0.25\ a_0$ in eqn (13).

B. Bound state calculations

Ro-vibrational bound state calculations for different J states with e and f symmetries are carried out in scattering coordinates using the 3D discrete variable representation (DVR) method with the DVR3D program suite.[38] The radial Gauss-Laguerre quadrature grids consist of 86 and 32 points along the R and r coordinates, respectively. For the Jacobi angle θ, a grid of 36 Gauss-Legendre points was used and for the radial grids (r, R) the wavefunctions were constructed using Morse oscillator functions. For the diatom (H_2^+), $r_e = 2.5\ a_0$, $D_e = 0.1026\ E_h$ and $\omega_e = 0.018\ E_h$ are used and with these parameters the r-grid covered points between 0.92 to 3.8 a_0. As the wave functions for the near-dissociation states need to cover large values along R, the corresponding values were $R_e = 11.5\ a_0$, $D_e = 0.08\ E_h$, and $\omega_e = 0.00065\ E_h$ which defined the R grid between 1.82 and 20.87 a_0. The r_2 embedding[38] is used to calculate the rotationally excited states, where the z-axis is parallel to R in body-fixed Jacobi coordinates. For the $J > 0$ calculations, the Coriolis couplings are included. In the r_2 embedding, calculations with ipar = 1 and 0 correspond to the *ortho* and *para* H_2^+, respectively. The e and f symmetries are assigned by the parity operator p.

Another method by which we calculated the bound states is the coupled-channels variational method (CCVM). It is similar to a coupled-channels (CC) scattering calculation, but instead of propagating the radial coordinate R to solve the CC differential equations it uses a basis also in R and obtains the desired number of eigenstates of the Hamiltonian matrix with the iterative Davidson algorithm.[39] For the angular motion of H_2^+ in the H_2^+–He complex we used a free rotor basis with $j_{H_2^+}$ ranging from 0 to 14 (or 16, in tests). The basis in the H_2^+ vibrational coordinate r contains the v = 0–7 eigenfunctions of the free H_2^+ Hamiltonian for $j_{H_2^+} = 0$ on a grid of 110 equidistant points with r = 0.25–5.5 a_0. The basis in R was obtained by solving a one-dimensional (1D) eigenvalue problem with the radial kinetic energy and a potential $V_{\text{eff}}(R)$. This potential is a cut through the full 3D potential of H_2^+–He with θ and r fixed at the equilibrium values, to which we added a term linear in R with a slope that was variationally optimized by using the R basis in full 3D calculations of the lower H_2^+–He levels. The 1D radial eigenvalue problem was solved with sinc-DVR[40] on a 357-point grid with R = 2 to 50 a_0. In order to converge also near-dissociative states we finally included 120 radial basis functions in the 3D full direct product basis.

In all bound state calculations the atomic masses were m_H= 1.00782503 and m_{He} = 4.00260325 amu, respectively,[41] which differ slightly from those used in earlier bound state and scattering calculations which employed m_H = 1.00727647 amu and m_{He} = 4.00234755 amu.[42] These differences lead to shifts in the bound states by ∼ 0.5 cm^{-1}, see Table S6 (ESI†). The states in the present work are labeled with respect to the H_2^+ quantum numbers v and j for the vibrational and rotational state of the diatomic, and J for the spin-free orbital angular momentum of the complex. The fine and hyperfine splittings due to coupling of electron and total nuclear spin, and coupling of the resultant to the rotational angular momentum of the nuclei are both less than 100 MHz, so are several orders of magnitude smaller than the separation between rotational levels of the complex. Thus, identification of N (used in experiments[12]) with J is a meaningful approximation. It is also worthwhile to mention that for *ortho*- and *para*-H_2^+ the dissociation limits for the complex differ due to the different nuclear spins for the two spin isomers (0 for *para* and 1 for *ortho*). For *para*-H_2^+ only even j-states are allowed and the complex dissociates to E = 0 whereas for *ortho*-H_2^+ only odd j-states exist and the complex dissociates to the j = 1 state of H_2^+ with an energy of 2B, where B is the rotational constant. For the MRCI+Q and FCI PESs the dissociation limits for *ortho*-H_2^+ are 58.2320 cm^{-1} and 58.2336 cm^{-1}, respectively.

III. Results and discussion

A. Quality of the PESs

First, the quality of the *ab initio* calculations and their RKHS representation is considered. In Fig. 3 the analytical energies are compared with the *ab initio* energies for a few selected Jacobi angles at r = 2.0 a_0 for the MRCI+Q+LR PES. A similar comparison is also shown for the FCI PES in Fig. S1 (ESI†). Excellent agreement between the two sets of data is found, see Fig. 3. Fig. S2 (ESI†) presents the contour plot of the analytical energies for the H_2^+–He system for r = 2.0 a_0.

The quality of the RKHS representation of the MRCI+Q+LR and FCI PES is reported in Fig. S3 (ESI†). For the grid points

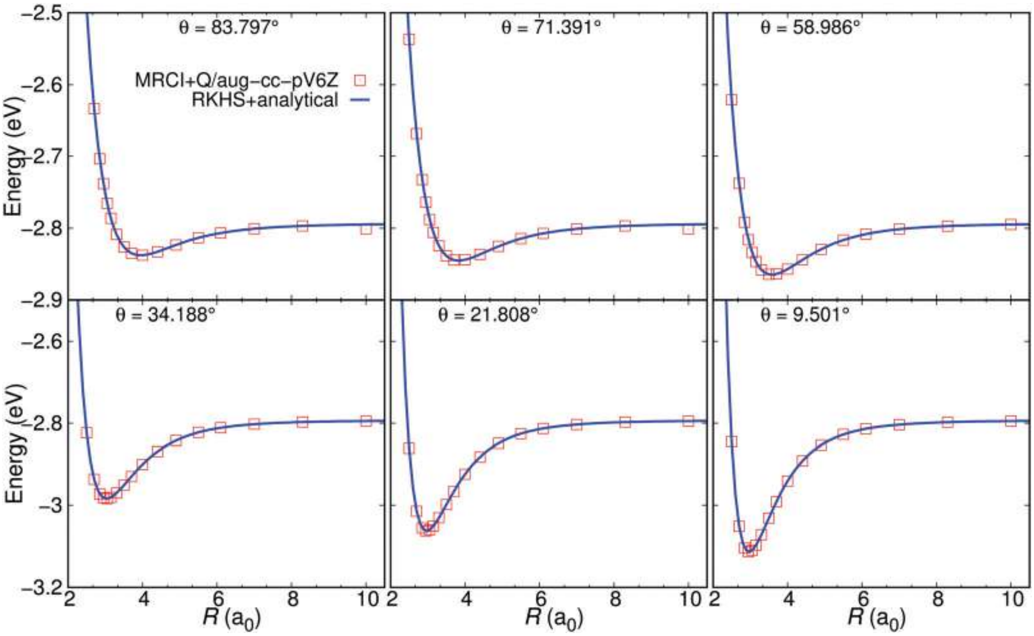

Fig. 3 The analytical energies at off-grid points from the MRCI+Q+LR PES (solid line) and the MRCI+Q/aug-cc-pV6Z *ab initio* energies (open symbols) as a function of R for several Jacobi angles and at fixed r = 2.0 a_0. The two points at long range ($R \sim 10\ a_0$ for θ = 83.797° and θ = 71.391°) are due to convergence problems with MRCI+Q, see also Fig. 1.

used to generate the RKHS representation, the agreement between reference points and the reproducing kernel is excellent with R^2 values of $(1.0-8 \times 10^{-10})$ and $(1.0-2 \times 10^{-12})$ for MRCI+Q+LR and FCI PESs, respectively. The root mean squared errors (RMSE) for the training data set are 0.67 and 0.02 cm^{-1} for the MRCI+Q+LR and FCI PESs, respectively. In addition, *ab initio* energies were also calculated at the MRCI+Q/aug-cc-pV6Z and FCI/aug-cc-pV5Z level of theory for off-grid geometries. They are also reported in Fig. S4 (ESI†) together with the RKHS energies evaluated at these geometries. Again, the agreement between the electronic structure calculations and the RKHS representation is good with RMSEs of 2.16 cm^{-1} for the MRCI+Q+LR PES and 0.92 cm^{-1} for the FCI PES.

The equilibrium geometry of the FCI/aug-cc-pV5Z surface is a linear He–H–H configuration (r_e = 2.07494 a_0 and R_e = 2.97120 a_0), with an energy of −2735.11 cm^{-1} below the H_2^+ asymptote. This compares with the MRCI+Q+LR calculations for which r = 2.07447 a_0, R = 2.97127 a_0 and depth −2736.17 cm^{-1} and the earlier QCISD(T)/aug-cc-pvQz PES[15] (r = 2.0750 a_0, R = 2.9720 a_0 and depth −2717.0 cm^{-1}) values. For comparison, the refined PES from ref. 18 supports a linear equilibrium structure with a depth of −2732.34 cm^{-1} and r_e = 2.07792 a_0 and R_e = 2.96596 a_0. Hence, the structures of all PESs differ by less than 0.01 a_0 but the energetics varies over a range of ∼20 cm^{-1} whereas the dissociation energies for the two PESs from the present work only differ by 1.1 cm^{-1}.

B. Bound states

The ground state energy of $H_2^+(v = 0, j = 0)$–He computed from the MRCI+Q+LR surface for *ortho*-H_2^+–He using DVR3D and CCVM are −1795.1567 and −1795.3328 cm^{-1}, respectively. The same energies, are obtained from the FCI PES as −1793.7632 and −1793.9067 cm^{-1}, using DVR3D and CCVM, respectively. These values are ∼40 cm^{-1} lower compared to those reported previously[15] (−1754.269 cm^{-1}) on the QCISD(T) PES. In ref. 15 only 3 quadrature points along r were used for the 3D bound state calculations, which may not be sufficient to fully converge the energies. The ground state energy is also calculated in the present work following a time dependent wave packet approach[43] on a 2D potential fixing r at 2.0 a_0. These ground state energies are in fair agreement with previous results (−1603 *vs.* −1593 cm^{-1}).[15]

For *para*-H_2^+–He the ground state energies obtained from the MRCI+Q+LR PES using DVR3D and CCVM are −1795.1575 and −1795.3352 cm^{-1}, respectively. For the FCI surface the ground state energies of *para*-H_2^+–He are calculated as −1793.7639 and −1793.9091 cm^{-1} using DVR3D and CCVM, respectively. The difference between DVR3D and CCVM is less than 0.17 cm^{-1} for both, *ortho* and *para*-H_2^+–He. For the FCI+LR PES all the bound states obtained from different methods for both, *ortho* and *para*-H_2^+–He are within 0.02 cm^{-1} or less of the FCI PES results. Hence, only the results obtained from the MRCI+Q+LR and FCI PESs are reported.

A direct comparison for all and the near-dissociative (within 20 cm^{-1} of dissociation) bound e states for *ortho*-H_2^+–He and J = 0 to J = 6 from DVR3D calculations and using the MRCI+Q+LR (red) and FCI (black) PESs is given in Fig. 4 and 5. All states up to the dissociation limit of v = 0, j = 1 state of H_2^+ are reported. The level pattern for the two PESs is nearly identical. The distribution of the energy difference ΔE between the MRCI+Q+LR and the FCI PESs for calculations with DVR3D or CCVM is given in Fig. S5 (ESI†).

The transitions that were probed by the microwave experiments lie close to dissociation. Hence, a particular focus here is

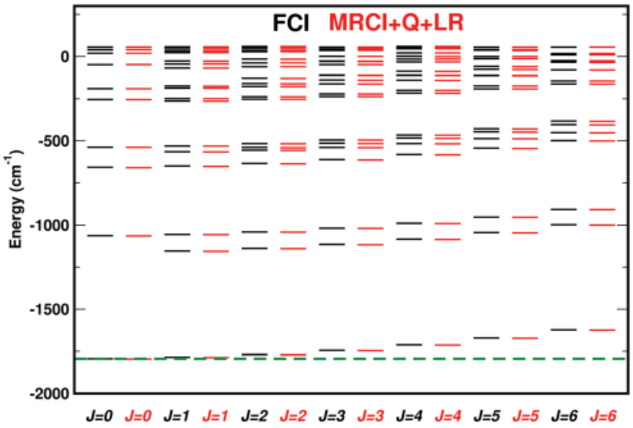

Fig. 4 Bound state energies for J = 0 to 6 for *ortho*-H_2^+–He with e symmetry computed from DVR3D calculations. Results on the MRCI+Q+LR surface (red) and FCI (black) are shown. The ground state energy (−1793.7632 cm^{-1}) for the FCI/aug-cc-pv5Z surface is marked with a dashed line.

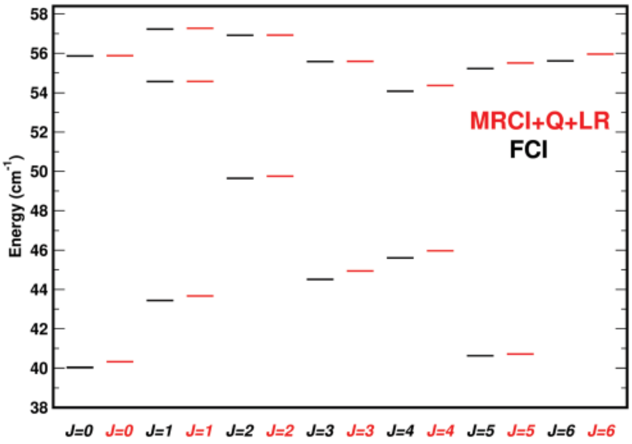

Fig. 5 Same as Fig. 4 except for the near dissociation states. States within ∼20 cm^{-1} of the dissociation are reported.

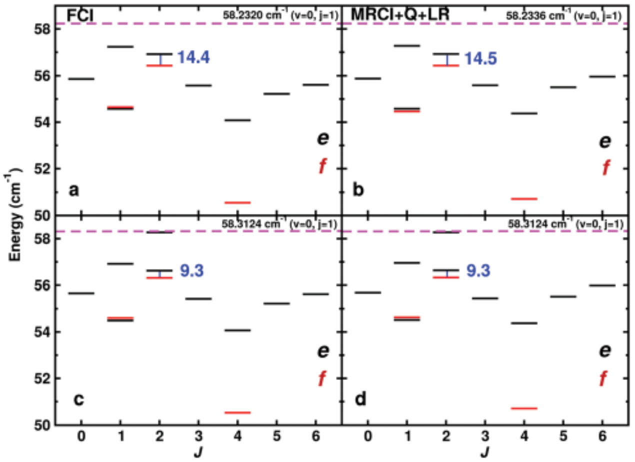

Fig. 6 Near dissociation *ortho*-H_2^+–He states (in cm^{-1}) and predicted transition frequencies in (GHz) using the FCI (left, panels a and c) and MRCI+Q+LR (right, panels b and d) PESs. States with e (black) and f symmetry (red) are reported separately. Results from DVR3D and CCVM are in the top and bottom row, respectively. The 14.4 GHz (MRCI+Q+LR, DVR3D), 14.5 GHz (FCI, DVR3D) and 9.3 (both PESs, CCVM) GHz parity doublet is a candidate for the 15.2 GHz line observed experimentally which had been assigned to a parity doublet with ΔN = 0.[12]

on accurately computing these stationary states and to determine whether any candidate transitions can be identified from using the MRCI+Q+LR and the FCI PESs. A tentative assignment in particular for the 15.2 GHz and 21.8 GHz transitions has been given previously based on experiments using electric field dissociation.[12] They were analyzed using an effective Hamiltonian. The 15.2 GHz transition was assigned to a low-N transition (in the terminology of ref. 12, N is the spin-free angular momentum which is J in the present work) with ΔN = 0 with N = 3 or N = 4 in *ortho*-H_2^+–He. In the following, N is used when referring to the analysis of the experiments[12] whereas J is used when discussing the present calculations.

For the 21.7 GHz transition on the other hand the analysis led to an assignment involving ΔN = 1 with N = 11 and N' = 10 in *para*-H_2^+–He. While the analysis leading to a ΔN = 1 transition involving *para*-H_2^+ is based on physical grounds, that to a high-N state involves fitting of the Zeeman pattern which is more approximate. The selection rules for these transitions are e ↔ f for ΔJ = 0 and e ↔ e or f ↔ f for ΔJ = ±1, respectively.

First, the near-dissociative states for *ortho*-H_2^+–He are discussed. All near-dissociative states from the MRCI+Q+LR and FCI PESs using the DVR3D and CCVM methods are reported in Fig. 6a–d. All energies for J = 0 to 6 are also reported in Tables 2 and 3. There is one e/f parity doublet with ΔJ = 0 with a transition frequency between 10 and 18 GHz, involving the J = 2 state for *ortho*-H_2^+–He. Using DVR3D the transition frequency is 14.4(5) GHz whereas with the CCVM code the

Table 2 Near dissociation states calculated using MRCI surface with DVR3D and CCVM for H_2^+–He in cm^{-1}. Zero is set to the energy of H_2^+(v = 0, j = 0) state. The dissociation limit for *ortho* is at 58.2336 cm^{-1} and 58.3124 cm^{-1} for the DVR3D and CCVM respectively, which corresponds to H_2^+(v = 0, j = 1), whereas the dissociation limit for *para*- is at 0 cm^{-1} which corresponds to H_2^+(v = 0, j = 0)

	ortho				*para*			
	e		f		e		f	
J	CCVM	DVR3D	CCVM	DVR3D	CCVM	DVR3D	CCVM	DVR3D
0	39.896	40.321			−15.641	−15.719		
	55.689	55.876			−1.509	−1.137		
1	43.199	43.668	54.629	54.464	−13.965	−14.035		
	54.514	54.582			−0.954	−0.430		
	56.959	57.273						
2	49.345	49.755	56.329	56.439	−10.712	−10.766		
	56.639	56.923			−0.061	0.895		
	58.272	59.186						
3	44.938	44.941	41.798	41.783	−6.082	−6.109		
	55.443	55.588						
4	46.022	45.971	50.718	50.712	−0.587	−0.540		
	54.375	54.375						
5	40.655	40.711	40.682	40.680	−7.877	−7.799		
	55.518	55.507						
6	55.985	55.959					−13.897	−13.746

Table 3 Near dissociation states calculated using FCI surface with DVR3D and CCVM for H_2^+–He in cm^{-1}. Zero is set to the energy of $H_2^+(v = 0, j = 0)$ state. The dissociation limit for *ortho* is at 58.2320 cm^{-1} and 58.3124 cm^{-1} for the DVR3D and CCVM respectively, which corresponds to $H_2^+(v = 0 j = 1)$, whereas the dissociation limit for *para* is at 0 cm^{-1} which corresponds to $H_2^+(v = 0, j = 0)$

	ortho				*para*			
	e		f		e		f	
J	CCVM	DVR3D	CCVM	DVR3D	CCVM	DVR3D	CCVM	DVR3D
0	39.575	40.036			−16.005	−16.067		
	55.662	55.860			−1.527	−1.150		
1	42.934	43.438	54.601	54.648	−14.315	−14.368		
	54.494	54.575			−0.969	−0.448		
	56.916	57.232						
2	49.213	49.647	56.314	56.437	−11.021	−11.058		
	56.623	56.916			−0.061	0.881		
	58.271	59.162						
3	44.497	44.513	41.473	41.473	−6.311	−6.320		
	55.422	55.577						
4	45.652	45.611	50.538	50.547	−0.680	−0.619		
	54.067	54.084						
5	40.565	40.626	40.854	40.860	−8.092	−8.005		
	55.219	55.220						
6	55.626	56.610					−11.890	−11.742

transition is at 9.3 GHz. The parity doublet in both cases is within 2 cm^{-1} of dissociation which makes it a pair of near-dissociative states. This is also confirmed by considering the expectation value for the R-coordinate for the two states involved which are $\langle R \rangle = 13.1\ a_0$ for the e state and $\langle R \rangle = 12.7\ a_0$ for the f state which confirms their long range character as suggested from the experiments.

Next, the near-dissociative states for *para*-H_2^+–He are discussed for the two PESs and the two methods to compute bound states, see Fig. 7a–d. The only near-dissociative states involving either an e/e or an f/f transition with a transition frequency around 20.1(2) and 16.7(6) GHz from DVR3D and CCVM involves a $J = 0$ and a $J = 1$ state. The $\langle R \rangle = 15.0\ a_0$ for the $J = 0$, e state and $\langle R \rangle = 16.0\ a_0$ for the $J = 1$, f state, show the long range nature of the wave functions. The potential candidate for the 21.8 GHz transition is not found for the high J states sufficiently close to dissociation to be part of a suitable candidate transition.

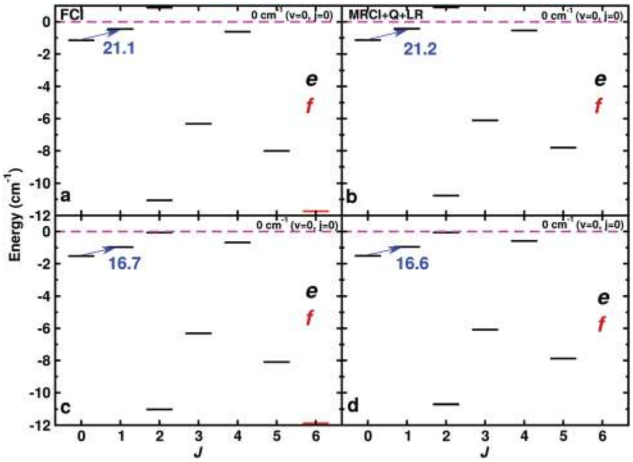

Fig. 7 Near dissociation *para*-H_2^+–He states (in cm^{-1}) and predicted transition frequencies in (GHz) using the FCI (left, panels a and c) and MRCI+Q+LR (right, panels b and d) PESs. States with e (black) and f symmetry (red) are reported separately. Results from DVR3D and CCVM are in the top and bottom row, respectively.

IV. Discussion and conclusions

Two new PESs at the MRCI+Q+LR and FCI level of theory with large basis sets and represented as a reproducing kernel have been used to determine all bound and near-dissociative states for *ortho*- and *para*-H_2^+–He. Although MRCI+Q is already a high level of electronic structure theory, it was found to break down for H_2^+–He separations longer than $R \sim 10\ a_0$, see Fig. 1 and 3. For this part of the MRCI PES an analytical long range potential was used. In order to establish that such an approach is meaningful, the full 3d PES was calculated at the even higher full CI level of theory. It is found that at both levels of theory the bound states compare to within fractions of a wavenumber when stationary states are determined from the same nuclear quantum code, see Table S5 (ESI†). Moreover, the stationary states on one and the same PES determined from two different quantum bound state codes (DVR3D and CCVM) also agree closely, typically within less than fractions of one cm^{-1}.

The need for such new PESs can also be gleaned from Table S6 (ESI†) which compares the $J = 0$ bound states for *para*-H_2^+–He on the FCI PES with three different methods and compares them with results on the earlier, high-quality PES used in previous work.[18,42] The dissociation energies between the present and previous[18] PESs differ only by about 3 cm^{-1} whereas the lower bound states differ rather by 20 cm^{-1}. This suggests that the shape of the PESs away from the minimum differs also due to the different long range behaviour of the present and previous PESs. This is also supported by the observation that the total number of bound states on the present and previous PESs differs by one, *i.e.* one near-dissociative state is missing. Furthermore, the table also shows that three different methods for computing bound states (DVR3D, CCVM and time-dependent wave packet (TDWP)[43]) yield stationary states that differ by ∼0.3 cm^{-1} or less.

The present computations provide stringent benchmarks on potential transitions that have been observed experimentally. One such assignment is for the 15.2 GHz transition which corresponds to *ortho*-H_2^+–He. The transition found in the present work involves an e/f parity doublet with $J = 2$. This compares with a tentative assignment to an e/f parity doublet involving either a $J = 3$ or $J = 4$ state. For the 21.8 GHz transition which had been tentatively assigned to an e/e or f/f transition in *para*-H_2^+–He the candidate, near-dissociation states are $J = 0$ and $J = 1$, both of which are within less than 2 cm^{-1} of dissociation and the transition frequencies range from 16 to 22 GHz. However, no high-J candidate states suitable to assign the experimentally observed transition were found.

This work presents the generation and representation of two high-accuracy, full dimensional PESs for H_2^+–He together with quantum bound state calculations that provide first potential assignments of experimentally characterized, near-dissociation states. The results from both, MRCI+Q+LR and full CI PESs, using two different approaches for calculating the quantum bound states are largely consistent. It will be interesting to use the present PESs in future inelastic scattering calculations.

Code availability

The code for the RKHS PESs has been made available on github.[44]

Conflicts of interest

There are no conflicts of interest to declare.

Acknowledgements

This work was supported by the Swiss National Science Foundation through grants 200021-117810, the NCCR MUST and the AFOSR (to MM). The authors thank Prof. J. Tennyson for exchange on the DVR3D program.

References

1 A. G. G. M. Tielens, *Rev. Mod. Phys.*, 2013, **85**, 1021.
2 Q. Li, J. Jiang and J. Hao, *KONA Powder Part. J.*, 2015, 57–74.
3 R. Güsten, H. Wiesemeyer, D. Neufeld, K. M. Menten, U. U. Graf, K. Jacobs, B. Klein, O. Ricken, C. Risacher and J. Stutzki, *Nature*, 2019, **568**, 357–359.
4 B. Zygelman, P. C. Stancil and A. Dalgarno, *Astrophys. J.*, 1998, **508**, 151–156.
5 J. H. Black, *Philos. Trans. R. Soc., A*, 2012, **370**, 5130–5141.
6 S. Lepp, P. C. Stancil and A. Dalgarno, *J. Phys. B: At., Mol. Opt. Phys.*, 2002, **35**, R57–R80.
7 M. H. Vera, F. A. Gianturco, R. Wester, H. da Silva, Jr., O. Dulieu and S. Schiller, *J. Chem. Phys.*, 2017, 146.
8 J. C. J. Koelemeij, B. Roth, A. Wicht, I. Ernsting and S. Schiller, *Phys. Rev. Lett.*, 2007, **98**, 173002.
9 S. Schiller, D. Bakalov and V. I. Korobov, *Phys. Rev. Lett.*, 2014, **113**, 023004.
10 A. Klein, Y. Shagam, W. Skomorowski, P. S. Zuchowski, M. Pawlak, L. M. C. Janssen, N. Moiseyev, S. Y. T. van de Meerakker, A. van der Avoird, C. P. Koch and E. Narevicius, *J. Chem. Phys.*, 2017, **13**, 35–38.
11 A. Carrington, D. I. Gammie, A. M. Shaw, S. M. Taylor and J. M. Hutson, *Chem. Phys. Lett.*, 1996, **260**, 395–405.
12 D. I. Gammie, J. C. Page and A. M. Shaw, *J. Chem. Phys.*, 2002, **116**, 6072.
13 T. Joseph and N. Sathyamurthy, *J. Chem. Phys.*, 1987, **86**, 704–714.
14 M. F. Falcetta and P. E. Siska, *Mol. Phys.*, 1999, **97**, 117–125.
15 M. Meuwly and J. M. Hutson, *J. Chem. Phys.*, 1999, **110**, 3418.
16 P. Palmieri, C. Puzzarini, V. Aquilanti, G. Capecchi, S. Cavalli, D. de Fazio, A. Aguilar, X. Giménez and J. M. Lucas, *Mol. Phys.*, 2000, **98**, 1835–1849.
17 C. Ramachandran, D. D. Fazio, S. Cavalli, F. Tarantelli and V. Aquilanti, *Chem. Phys. Lett.*, 2009, **469**, 26–30.
18 D. de Fazio, M. de Castro-Vitores, A. Aguado, V. Aquilanti and S. Cavalli, *J. Chem. Phys.*, 2012, **137**, 244306.
19 H.-J. Werner and P. J. Knowles, *J. Chem. Phys.*, 1988, **89**, 5803–5814.
20 P. J. Knowles and H.-J. Werner, *Chem. Phys. Lett.*, 1988, **145**, 514–522.
21 A. K. Wilson, T. van Mourik and T. H. Dunning, *THEOCHEM*, 1996, **388**, 339–349.
22 P. J. Knowles and N. Handy, *Chem. Phys. Lett.*, 1984, **111**, 315–321.
23 P. J. Knowles and N. C. Handy, *Comput. Phys. Commun.*, 1989, **54**, 75–83.
24 T. H. Dunning, *J. Chem. Phys.*, 1989, **90**, 1007–1023.
25 D. E. Woon and T. H. Dunning, *J. Chem. Phys.*, 1994, **100**, 2975–2988.
26 H.-J. Werner and P. J. Knowles, *J. Chem. Phys.*, 1985, **82**, 5053–5063.
27 P. J. Knowles and H.-J. Werner, *Chem. Phys. Lett.*, 1985, **115**, 259–267.
28 H.-J. Werner and W. Meyer, *J. Chem. Phys.*, 1980, **73**, 2342–2356.
29 H.-J. Werner, P. J. Knowles, G. Knizia, F. R. Manby and M. Schütz, *Wiley Interdiscip. Rev.: Comput. Mol. Sci.*, 2012, **2**, 242–253.
30 A. J. C. Varandas, *Intermolecular and Intramolecular Potentials: Topographical Aspects, Calculation, and Functional Representation via A Double Many-Body Expansion Method*, John Wiley & Sons, Inc., 2007, pp. 255–338.
31 A. Aguado and M. Paniagua, *J. Chem. Phys.*, 1992, **96**, 1265–1275.
32 D. M. Bishop and J. Pipin, *Chem. Phys. Lett.*, 1995, **236**, 15.
33 L. Velilla, B. Lepetit, A. Aguado, A. Beswick and M. Paniagua, *J. Chem. Phys.*, 2008, **129**, 084307.
34 W. H. Press, S. A. Teukolsky, W. T. Vetterling and B. P. Flannery, *Numerical Recipes in Fortran 77*, Cambridge University Press, New York, 1992.
35 T.-S. Ho and H. Rabitz, *J. Chem. Phys.*, 1996, **104**, 2584.
36 O. T. Unke and M. Meuwly, *J. Chem. Inf. Model*, 2017, **57**, 1923–1931.
37 B. Yang, P. Zhang, C. Qu, X. H. Wang, P. C. Stancil, J. M. Bowman, N. Balakrishnan, B. M. McLaughlin and R. C. Forrey, *J. Phys. Chem. A*, 2018, **122**, 1511–1520.
38 J. Tennyson, M. A. Kostin, P. Barletta, G. J. Harris, O. L. Polyansky, J. Ramanlal and N. F. Zobov, *Comput. Phys. Commun.*, 2004, **163**, 85–116.
39 E. R. Davidson, *J. Comput. Phys.*, 1975, **17**, 87.
40 G. C. Groenenboom and D. T. Colbert, *J. Chem. Phys.*, 1993, **99**, 9681–9696.
41 P. Linstrom and W. Mallard, NIST Webbook (NIST Chemistry Webbok, NIST Standard Reference Database Number 69), ed. P. J. Lindstrom and W. G. Mallard, http://webbook.nist.gov, National Institute of Standards and Technology, Gaithersburgh MD, 20899, 2019.
42 T. Szidarovszky and K. Yamanouchi, *Mol. Phys.*, 2017, **115**, 1916–1926.
43 D. Koner, L. Barrios, T. González-Lezana and A. N. Panda, *J. Chem. Phys.*, 2016, **144**, 034303.
44 https://github.com/MeuwlyGroup/H2pHe.